

WPPNets and WPPFlows: The Power of Wasserstein Patch Priors for Superresolution

Fabian Altekrüger^{†*} Johannes Hertrich[†]

May 6, 2022

Abstract

Exploiting image patches instead of whole images have proved to be a powerful approach to tackle various problems in image processing. Recently, Wasserstein patch priors (WPP), which are based on the comparison of the patch distributions of the unknown image and a reference image, were successfully used as data-driven regularizers in the variational formulation of superresolution. However, for each input image, this approach requires the solution of a non-convex minimization problem which is computationally costly. In this paper, we propose to learn two kinds of neural networks in an unsupervised way based on WPP loss functions. First, we show how convolutional neural networks (CNNs) can be incorporated. Once the network, called WPPNet, is learned, it can very efficiently applied to any input image. Second, we incorporate conditional normalizing flows to provide a tool for uncertainty quantification. Numerical examples demonstrate the very good performance of WPPNets for superresolution in various image classes even if the forward operator is known only approximately.

1 Introduction

In inverse problems, the task is to reconstruct an unknown ground truth x from a noisy observation

$$y = f(x) + \xi, \quad (1)$$

where f is an ill-posed forward operator and ξ is the realization of white Gaussian noise with distribution $\mathcal{N}(0, \sigma^2 I)$. Such problems can be tackled by finding a minimizer of a variational problem

$$\mathcal{J}(x) = D(f(x), y) + \lambda \mathcal{R}(x), \quad \lambda > 0, \quad (2)$$

where $D(f(x), y)$ is a data-fidelity term which accounts for the noise and \mathcal{R} a regularizer or image prior. The concrete form of (2) is often derived by a Bayesian approach.

*Department of Mathematics, Humboldt-Universität zu Berlin, Unter den Linden 6, D-10099 Berlin, Germany, fabian.altekrueger@hu-berlin.de

†Institute of Mathematics, Technische Universität Berlin, Straße des 17. Juni 136, D-10623 Berlin, Germany, j.hertrich@math.tu-berlin.de.

In this paper, we focus on the problem of superresolution. Here, x is a high-resolution image and y a low-resolution image obtained by a forward operator f , which is usually a composition of a blur operator and a downsampling operator. Due to its actuality, superresolution using deep neural networks (NNs) was considered in many papers, see e.g., [14, 38, 48, 49, 54, 58, 64], see also [61] for a survey. However, within their training process, these methods require the access to a large amount of registered pairs (x_i, y_i) of high- and low-resolution images. Only very few NN based approaches make use of the forward operator f instead of large training data sets. Examples are the zero-shot superresolution [52], the deep image prior [55] and Plug-and-Play methods [57]. Zero-shot superresolution [52] exploits the internal image statistics and learns image-specific relations between the low-resolution image and its downsampled versions in order to apply these relations for reconstructing the high-resolution image. The Deep Image Prior (DIP) [55] learns a CNN by minimizing the loss function

$$\mathcal{L}_{\text{DIP}}(\theta) := \|f(G_\theta(z)) - y\|^2,$$

where z is a randomly chosen input and an early-stopping technique is used as regularization. Then, the reconstructed image is obtained by $x = G_\theta(z)$. It was shown in [55] that DIP admits competitive results for many inverse problems. In [4] a combination of DIP with the TV regularizer (DIP+TV), leading to the loss function

$$\mathcal{L}_{\text{DIP+TV}}(\theta) := \|f(G_\theta(z)) - y\|^2 + \lambda \text{TV}(G_\theta(z)), \quad \lambda > 0,$$

was successfully proposed for computerized tomography. Note that each reconstruction with DIP+TV requires the training of a NN, which makes the method time consuming. The idea of Plug-and-Play methods is to consider an optimization algorithm from convex analysis for solving (2), as, e.g., the forward-backward splitting [9] or the alternating direction method of multipliers [10, 15], and to replace the proximal operator with respect to the regularizer by a more general denoiser. For example, the forward backward splitting algorithm for minimizing (2) is given by

$$x_{r+1} = \text{prox}_{\eta R}(x_r - \eta \nabla_x D(x_r, y))$$

and can be modified by

$$x_{r+1} = \mathcal{G}(x_r - \eta \nabla_x D(x_r, y)), \quad (3)$$

where \mathcal{G} is a neural network trained for denoising natural images as the DRUNet from [62]. Plug-and-Play methods were used for several applications in image processing with excellent performance, see e.g., [6, 20, 25, 42, 43, 62]. Closely related to Plug-and-Play methods are regularizing by denoising (RED) [47], variational networks [16] and total deep variation [33].

On the other hand, powerful methods based on the self-similarity of small patches within natural images were developed in the last years. Such patch-based methods were used, e.g., for denoising [5, 27, 36, 51] and superresolution [26, 50]. In particular, the expected patch log-likelihood algorithm (EPLL) [44, 65] achieved competitive results to NNs by using the log-likelihood function of a Gaussian mixture model as regularizer

within the variational problem (2). Recently, this approach was also extended to posterior sampling for uncertainty quantification [19].

In this paper, we assume that we are given the (approximate) forward operator f , a data base of low resolution images y_1, \dots, y_m and only one single high-resolution reference image \tilde{x} . Further, we assume that the distribution of patches in \tilde{x} is similar to the patch distribution in the unknown high-resolution ground truths x_1, \dots, x_m corresponding to y_1, \dots, y_m . This assumption is fulfilled for images from similar image classes as, e.g., from textures or materials. The setting is motivated by the analysis of materials microstructures. Here, it is usually possible to scan a large area of a material with a low resolution, while the limited amount of time and resources forbids to image the same size of a data using a higher resolution. Further, it is often impossible to scan the same section of one sample twice with different resolutions as in many applications destructive imaging processes, e.g., FIB-SEM are used. These imaging techniques destroy the scanned section of the material and consequently there is no chance to generate labeled training data. Within this setting, Hertrich et al. [24] proposed to solve the variational problem (2) using a so-called Wasserstein patch prior (WPP), which penalizes the quadratic Wasserstein distance between the patch distribution of x and the reference image \tilde{x} . The approach was inspired by the idea that a texture-like image can be represented by the distribution of small patches [17, 21, 28, 29, 37], which was used by Houdard et al. [29] to synthesize textures. A similar comparison of the Wasserstein-2 distance of patch distributions was used within a supervised setting in [45]. Unfortunately, the minimization of the corresponding variational problem requires several computations and differentiations of Wasserstein distances, which is computationally expensive. We propose to overcome this computational overhead by exploiting NNs. First we introduce WPPNets, which are NNs trained in an unsupervised way using a new WPP-based loss function. Then, in order to measure the uncertainty within the reconstructions, we train conditional normalizing flows using a WPP-Kullback-Leibler-based loss function and call the resulting model WPPFlows. Normalizing flows [13, 32, 46] are learned diffeomorphisms to model complicated and high-dimensional probability distributions using a much simpler latent distribution. Applications to inverse problems were considered e.g., in [1, 12, 53]. We demonstrate the performance of our methods by several numerical examples on real-world data¹. It turns out that WPPNets outperform several methods as Plug-and-Play approaches and DIP. In practice, it is often unrealistic to assume that the forward operator f is known exactly. Instead, it can be described inaccurately or estimated on synthetic data. Our numerical examples show that WPPNets are much more stable under such perturbations of the operator than other approaches. Finally, our examples show that WPPFlows are a reasonable method to quantify the uncertainty within the reconstructions as they produce diverse and realistic images.

The paper is organized as follows: in Section 2, we briefly review the WPP approach from [24]. Then, in Section 3, we introduce WPPNets. Conditional normalizing flows are incorporated in Section 4 to get WPPFlows. In Section 5, we present numerical examples and compare our results with other methods. Finally, conclusions are drawn in Section 6.

¹The code is available at <https://github.com/FabianAltekrueger/WPPNets>.

2 The Wasserstein Patch Prior

Let $P_j: \mathbb{R}^{d_1 \times d_2} \rightarrow \mathbb{R}^{s_1 \times s_2}$, $j = 1, \dots, N$ denote the operator which extracts the j -th patch of size $s_1 \times s_2$ with $s_1 \ll d_1$, $s_2 \ll d_2$ from an image $x \in \mathbb{R}^{d_1 \times d_2}$. Resampling the image columnwise, we may consider $P_j: \mathbb{R}^d \rightarrow \mathbb{R}^s$, where $d := d_1 d_2$ and $s := s_1 s_2$. Then we define the *empirical patch distribution* μ_x of $x \in \mathbb{R}^d$ by

$$\mu_x = \frac{1}{N} \sum_{j=1}^N \delta_{P_j(x)},$$

where δ denotes the Dirac measure. The main assumption in the following models is that similarly structured images x and \tilde{x} have also similar empirical patch distributions. Based on the empirical patch distributions of an image x and a reference image \tilde{x} , we define the *Wasserstein Patch Prior* (WPP) as the squared Wasserstein-2 distance of the corresponding empirical patch distributions, i.e.,

$$W_2^2(\mu_x, \mu_{\tilde{x}}) := \min_{\pi \in \Pi(\mu_x, \mu_{\tilde{x}})} \sum_{j=1}^N \sum_{k=1}^{\tilde{N}} \|P_j(x) - P_k(\tilde{x})\|^2 \pi_{j,k},$$

where $\Pi(\mu_x, \mu_{\tilde{x}}) := \{\pi = (\pi_{j,k}) \in \mathbb{R}_{\geq 0}^{N \times \tilde{N}} : \sum_{j=1}^N \pi_{j,k} = \frac{1}{N}, \sum_{k=1}^{\tilde{N}} \pi_{j,k} = \frac{1}{\tilde{N}}\}$. Note that only all patches must have the same size, but not the images. We will frequently use the dual form of the Wasserstein distance

$$W_2^2(\mu_x, \mu_{\tilde{x}}) = \max_{\psi \in \mathbb{R}^{\tilde{N}}} \left(\frac{1}{N} \sum_{j=1}^N \psi^c(P_j(x)) + \frac{1}{\tilde{N}} \sum_{k=1}^{\tilde{N}} \psi_k \right), \quad (4)$$

where $\psi := (\psi_k)_{k=1}^{\tilde{N}}$ and $\psi^c(P_j(x)) := \min_{k \in \{1, \dots, \tilde{N}\}} \{\|P_j(x) - P_k(\tilde{x})\|^2 - \psi_k\}$ denotes the c -transform of ψ . In [24], the WPP is used as a regularizer in the variational problem

$$\mathcal{J}(x) := \frac{1}{2} \|f(x) - y\|^2 + \lambda W_2^2(\mu_x, \mu_{\tilde{x}}). \quad (5)$$

It was shown that (5) outperforms state-of-the-art methods for superresolution of material images. However, it requires the minimization of the functional (5) for each high-resolution image x we want to reconstruct from its low resolution counterpart, which is computationally costly. Therefore, in the next section we propose to learn a NN based on the above loss function and then to use this network to generate high resolution images in a fast way.

Finally, we give the following remark which will be important when introducing WPPFlows in Section 4 and has a stochastic motivation.

Remark 1. *Under the assumption that $P_{Y|X=x} = \mathcal{N}(f(x), \sigma^2 I)$, Bayes' theorem implies that maximizing the log-posterior distribution $\log(p_{X|Y=y}(x))$ corresponding to (1) can be*

written as

$$\begin{aligned}
\arg \max_x \log (p_{X|Y=y}(x)) &= \arg \max_x \log \frac{p_{Y|X=x}(y) p_X(x)}{p_Y(y)} \\
&= \arg \max_x \left\{ \log \left(\exp \left(-\|f(x) - y\|^2 / (2\sigma^2) \right) \right) + \log (p_X(x)) \right\} \\
&= \arg \min_x \left\{ \frac{1}{2} \|f(x) - y\|^2 + \sigma^2 \log (p_X(x)) \right\}.
\end{aligned}$$

For the prior

$$p_X(x) \sim \exp(-\rho W_2^2(\mu_x, \mu_{\tilde{x}})), \quad \rho := \frac{\lambda}{\sigma^2},$$

this gives the variational WPP model (5) provided that p_X is a density function. This is ensured by the following proposition.

Proposition 2. *The function $\varphi(x) := \exp(-\rho W_2^2(\mu_x, \mu_{\tilde{x}}))$ is integrable.*

The proof is given in Appendix A.

3 WPPNets

We assume that we are given a high-resolution reference image $\tilde{x} \in \mathbb{R}^{\tilde{d}}$ and several low resolution images $y_i \in \mathbb{R}^n$, $i = 1, \dots, m$, $n < d$. The corresponding high-resolution ground truth images $x_i \in \mathbb{R}^d$, $i = 1, \dots, m$ are unknown, but we assume that the x_i have a similar patch distribution as the reference image \tilde{x} . Based on (5) it appears natural to train a CNN G_θ using the loss function

$$\mathcal{L}(\theta) := \frac{1}{m} \sum_{i=1}^m \|f(G_\theta(y_i)) - y_i\|^2 + \lambda W_2^2(\mu_{G_\theta(y_i)}, \mu_{\tilde{x}}). \quad (6)$$

In other words, the network will be trained to map an observation y onto the corresponding MAP estimator x of X given $Y = y$ under the prior distribution defined by the density $p_X \propto \varphi$ in Proposition 2.

However, when training a CNN, usually small parts of the training images are used to ensure the computational efficiency. In this case, due to the smaller number of patches in the reconstructions, the similarity of the patch distributions is not longer clear. Therefore, we divide our training data into disjoint batches $(B_j)_j$ of size $|B_j| = b$, $j = 1, \dots, N_B$ with $\bigcup_{j=1}^{N_B} B_j = \{1, \dots, m\}$. Instead of comparing the patch distributions of \tilde{x} and y_j for each j separately, we now compare the patch distribution of \tilde{x} with the distribution of all patches within the images of the batch B_j . Formally, this corresponds to replacing in (6) the term

$$\frac{1}{|B_j|} \sum_{i \in B_j} W_2^2(\mu_{G_\theta(y_i)}, \mu_{\tilde{x}}) \quad \text{by} \quad W_2^2\left(\frac{1}{|B_j|} \sum_{i \in B_j} \mu_{G_\theta(y_i)}, \mu_{\tilde{x}}\right), \quad (7)$$

for $j = 1, \dots, N_B$. Then, we obtain the loss function

$$\mathcal{L}_{\text{WPPNet}}(\theta) := \frac{1}{|B|} \sum_{j=1}^{N_B} \frac{1}{b} \sum_{i \in B_j} \|f(G_\theta(y_i)) - y_i\|^2 + \lambda W_2^2\left(\frac{1}{b} \sum_{i \in B_j} \mu_{G_\theta(y_i)}, \mu_{\tilde{x}}\right). \quad (8)$$

We call a neural network trained with the loss function (8) a *Wasserstein Patch Prior Network* (WPPNet). The following lemma shows the relation between the terms in (7).

Lemma 3. *It holds*

$$\frac{1}{|B|} \sum_{i \in B} W_2^2(\mu_{G_\theta(y_i)}, \mu_{\tilde{x}}) \geq W_2^2\left(\frac{1}{|B|} \sum_{i \in B} \mu_{G_\theta(y_i)}, \mu_{\tilde{x}}\right),$$

so that $\mathcal{L}(\theta) \geq \mathcal{L}_{\text{WPPNet}}(\theta)$.

Proof. Using the dual form of the Wasserstein distance, we obtain

$$\begin{aligned} \frac{1}{|B|} \sum_{i \in B} W_2^2(\mu_{G_\theta(y_i)}, \mu_{\tilde{x}}) &= \frac{1}{|B|} \sum_{i \in B} \left(\max_{\psi \in \mathbb{R}^{\tilde{N}}} \frac{1}{N} \sum_{j=1}^N \psi^c(P_j(G_\theta(y_i))) + \frac{1}{\tilde{N}} \sum_{k=1}^{\tilde{N}} \psi_k \right) \\ &\geq \max_{\psi \in \mathbb{R}^{\tilde{N}}} \frac{1}{|B|} \sum_{i \in B} \left(\frac{1}{N} \sum_{j=1}^N \psi^c(P_j(G_\theta(y_i))) + \frac{1}{\tilde{N}} \sum_{k=1}^{\tilde{N}} \psi_k \right) \\ &= W_2^2\left(\frac{1}{|B|} \sum_{i \in B} \mu_{G_\theta(y_i)}, \mu_{\tilde{x}}\right). \end{aligned}$$

□

Remark 4. *To speed up the numerical computations, we replace the empirical patch distribution $\mu_{\tilde{x}}$ by the distribution of a random subset of all patches, i.e., we redefine $\mu_{\tilde{x}}$ as*

$$\mu_{\tilde{x}} = \frac{1}{|I|} \sum_{k \in I} \delta_{P_k(\tilde{x})},$$

where I is a random subset of $\{1, \dots, \tilde{N}\}$ of size $|I|$. For our numerical experiments we chose $|I| = 10000$.

In order to minimize the loss function (8) with a gradient-based optimization method, we need to compute the derivative of $W_2^2(\mu_{G_\theta(y)}, \mu_{\tilde{x}})$ with respect to θ for some observation $y \in \mathbb{R}^n$. To this end, recall that the Wasserstein distance reads in its dual form as

$$W_2^2(\mu_{G_\theta(y)}, \mu_{\tilde{x}}) = \max_{\psi \in \mathbb{R}^{\tilde{N}}} F(\psi, \theta; y), \quad F(\psi, \theta; y) := \frac{1}{N} \sum_{j=1}^N \psi^c(P_j(G_\theta(y))) + \frac{1}{\tilde{N}} \sum_{k=1}^{\tilde{N}} \psi_k.$$

Then the following well-known theorem provides a connection between the gradient of the Wasserstein distance and those of F , see, e.g., [29].

Theorem 5. *Let both $\theta \mapsto W_2^2\left(\frac{1}{N} \sum_{j=1}^N \delta_{P_j(G_\theta(y))}, \frac{1}{\tilde{N}} \sum_{k=1}^{\tilde{N}} \delta_{P_k(\tilde{x})}\right)$ and $\theta \mapsto F(\psi^*, \theta; y)$ be differentiable at θ_0 with $\psi^* \in \arg \max_{\psi} F(\psi, \theta_0; y)$. Then it holds*

$$\nabla_{\theta} W_2^2\left(\frac{1}{N} \sum_{j=1}^N \delta_{P_j(G_{\theta_0}(y))}, \frac{1}{\tilde{N}} \sum_{k=1}^{\tilde{N}} \delta_{P_k(\tilde{x})}\right) = \nabla_{\theta} F(\psi^*, \theta_0; y).$$

Since for almost every θ the set of minimizers

$$\kappa_\psi(j) = \arg \min_{k \in \{1, \dots, \tilde{N}\}} (\|P_j(G_\theta(y)) - P_k(\tilde{x})\|^2 - \psi_k)$$

is single-valued, it holds that $\psi^c(P_j(G_\theta(y))) = \|P_j(G_\theta(y)) - P_{\kappa_\psi(j)}(\tilde{x})\|^2 - \psi_{\kappa_\psi(j)}$, which is differentiable in θ if G_θ is. Thus, by Theorem 5, the gradient of the Wasserstein distance is given by

$$\begin{aligned} \nabla_\theta W_2^2(\mu_{G_\theta(y)}, \mu_{\tilde{x}}) &= \nabla_\theta F(\psi^*, \theta; y) \\ &= \frac{2}{N} \sum_{j=1}^N \left(\partial_\theta (P_j(G_\theta(y)))^\top \right) (P_j(G_\theta(y)) - P_{\kappa_{\psi^*}(j)}(\tilde{x})), \end{aligned}$$

where $\psi^* := \arg \max_{\psi \in \mathbb{R}^{\tilde{N}}} F(\psi, \theta; y)$. For computing ψ^* , we use a (stochastic) gradient ascent algorithm as suggested in [29].

4 WPPFlows

For several applications, it is crucial to get not only a realistic reconstruction x , but also to measure the uncertainty within the reconstruction. From a mathematical point of view this corresponds to reconstructing the full posterior distribution $P_{X|Y=y}$ instead of the MAP estimator within the Bayesian inverse problem

$$Y = f(X) + \Xi, \tag{9}$$

where $\Xi \sim \mathcal{N}(0, \sigma^2 I)$ is independent of X . For this purpose, we will make use of *conditional normalizing flows*. In particular, this allows to produce different possible high-resolution reconstructions from the same low-resolution image y .

Normalizing Flows The aim of normalizing flows is to sample from a complicated probability distribution P_X which admits the density function p_X . A *normalizing flow* $\mathcal{T} = \mathcal{T}_\theta: \mathbb{R}^d \rightarrow \mathbb{R}^d$ is an invertible neural network with parameters θ , which is learned to push forward a simple distribution P_Z (usually a standard Gaussian) to P_X such that $\mathcal{T}_\# P_Z = P_Z \circ \mathcal{T}^{-1} \approx P_X$. Several architectures of normalizing flows were proposed in literature [7, 18, 32, 46]. Here, we use an adaption of the SRFlow architecture [40] based on affine coupling blocks [3, 13]. A detailed description is given in Appendix C.

For applications in inverse problems, normalizing flows were generalized to incorporate a condition [2, 23]. More precisely, for approximating all posterior distributions $P_{X|Y=y}$ within the Bayesian inverse problem (9) using a flow model, we learn a mapping $\mathcal{T} = \mathcal{T}_\theta: \mathbb{R}^d \times \mathbb{R}^n \rightarrow \mathbb{R}^d$ such that for all $y \in \mathbb{R}^n$ we have that $\mathcal{T}(\cdot, y)$ is invertible and that $\mathcal{T}(\cdot, y)_\# P_Z \approx P_{X|Y=y}$. Note, that (conditional) normalizing flows can be generalized for the use of non-deterministic transformation, see the overview paper [22].

To ensure $\mathcal{T}(\cdot, y)_\# P_Z \approx P_{X|Y=y}$, we use the expectation on Y of the *backward Kullback-Leibler (KL) divergence*

$$\mathcal{L}(\theta) := \mathbb{E}_{y \sim P_Y} [\text{KL}(\mathcal{T}(\cdot, y)_\# P_Z, P_{X|Y=y})] \tag{10}$$

This was also proposed in [1, 23, 34, 53]. The KL divergence is not symmetric and for a discussion on forward versus backward Kullback-Leibler divergences we refer to [23].

For computing $\mathcal{L}(\theta)$ and taking its derivative, we use the following proposition, which can be deduced from [1, Prop. 1] and [3] by inserting the WPP as prior distribution.

Proposition 6. *Let X and Y be related by the Bayesian inverse problem (9). Then, for any $y \in \mathbb{R}^n$, the KL divergence $\text{KL}(\mathcal{T}(\cdot, y)_{\#}P_Z, P_{X|Y=y})$ is up to a constant equal to*

$$\mathbb{E}_{z \sim P_Z} \left[\frac{1}{2\sigma^2} \|f(\mathcal{T}(z, y)) - y\|^2 - \log(|\det(\nabla \mathcal{T}(z, y))|) + \rho W_2^2(\mu_{\mathcal{T}(z, y)}, \mu_{\tilde{x}}) \right]$$

By discretizing the expectation of P_Y by independent samples y_1, \dots, y_m of Y and using Proposition 6, the loss function from (10) is up to a constant equal to

$$\begin{aligned} \mathcal{L}(\theta) = \frac{1}{m} \sum_{i=1}^m \mathbb{E}_{z \sim P_Z} & \left[\frac{1}{2\sigma^2} \|f(\mathcal{T}(z; y_i)) - y_i\|^2 - \log |\det \nabla \mathcal{T}(z; y_i)| \right. \\ & \left. + \rho W_2^2(\mu_{\mathcal{T}(z; y_i)}, \mu_{\tilde{x}}) \right]. \end{aligned}$$

As in Section 3, we merge the patch distribution of a batch of images such that we obtain the loss function

$$\begin{aligned} \mathcal{L}_{\text{WPPFlow}}(\theta) := \mathbb{E}_{z_1, \dots, z_m \sim (P_Z)^m} & \left[\frac{1}{|B|} \sum_{j=1}^{N_B} \frac{1}{b} \sum_{i \in B_j} \frac{\|f(\mathcal{T}(z_i; y_i)) - y_i\|^2}{2\sigma^2} - \log |\det \nabla \mathcal{T}(z_i; y_i)| \right. \\ & \left. + \rho W_2^2\left(\frac{1}{b} \sum_{i \in B_j} \mu_{\mathcal{T}(z_i; y_i)}, \mu_{\tilde{x}}\right) \right]. \end{aligned}$$

We call a normalizing flow trained by this loss function *Wasserstein Patch Prior Flow* (WPPFlow).

5 Numerical Results

In this section we demonstrate the good performance of our methods. In Subsection 5.1 and 5.2, we assume that the forward operator f consisting of a blur operator and a downsampling operator is given exactly. Then, in Subsection 5.3, we demonstrate the robustness of WPPNets by assuming that the operator knowledge is inaccurate. In the first example, we generate the low-resolution data by a slightly different operator than we use for learning the WPPNet. In the second example, we consider real data, where the forward operator f is unknown. We estimate the forward operator f based on one pair of registered images and we use this (inaccurate) estimation of the operator for superresolution. Finally, in Subsection 5.4 we consider the uncertainty in reconstructing from a low-resolution image using WPPFlows. Details on the architecture and the experimental setup are given in Appendix B.

We compare our WPPNet with the following methods:

- bicubic interpolation [30].
- Plug-and-Play Forward Backward Splitting with DRUNet (PnP-DRUNet): we use the DRUNet from [62] as denoiser \mathcal{G} in (3) and run 100 iterations. Even with the learned NN, PnP-DRUNet is significantly slower than a simple evaluation of the WPPNet.
- Deep Image Prior with TV regularization (DIP+TV) [55]²: note that each reconstruction with the DIP+TV requires the training of a neural network. Thus, the reconstruction time of DIP+TV is much slower than for the WPPNet.
- CNN trained on natural images (CNNNat): a natural way to overcome the issue of missing (labeled) training data could be to train a CNN onto natural images and to hope that it generalizes to the special structured test set. Following this approach, we compare our results with an asymmetric CNN [54] trained on the 400 training images from the BSDS500 dataset [41]. As loss function, we use the standard L^2 -loss. Afterwards we apply these networks to our special structured test set. Training and reconstruction time of a CNNNat is comparable with those of a WPPNet.
- WPP from (5).

We have to emphasize that, except the WPP, these methods do not include some prior information and thus have some weaker assumptions than WPPNets. Nevertheless, there are not many comparison methods which include only one high-resolution image. The intention is to demonstrate the impact of including a comparably small knowledge about the underlying image domain.

To evaluate the quality of our results, we use three different quality measures:

- **PSNR**. For two images x and y on $[0, 1]^{m \times n}$, the peak-signal to noise ratio is defined as

$$\text{PSNR}(x, y) = -10 \log_{10} \left(\frac{1}{mn} \|x - y\|^2 \right).$$

Larger PSNR values correspond to a better reconstruction. It is well-known that the PSNR prefers very smooth reconstructions which does in general not coincide with the visual impression.

- **Blur effect** [11]. This metric is based on comparing an input image x with a blurred version x_{blur} . For sharp images x , the difference should be very pronounced while it will be small for blurred x . The blur effect is normalized to $[0, 1]$, where a small blur effect indicates that x is very sharp while a large blur effect means that x is very blurry.

²We use the original implementation from [55] available at <https://github.com/DmitryUlyanov/deep-image-prior>

- **LPIPS** [63]³ The basic idea of the learned perceptual image patch similarity is to compare the feature maps extracted from some deep neural network that is trained for some classical imaging task which is not necessarily related to our original problem. A small value of LPIPS indicates a high perceptual similarity.

Since we do not want to consider boundary effects, we do not consider a boundary of 40 pixels when evaluating the quality measures. All figures show the full images and zoomed-in parts below them.

5.1 Texture Superresolution

First, we consider the Kylberg texture dataset [35]⁴. Here, we use the textures "Grass" and "Floor". The high-resolution ground truth and the reference image are different 600×600 sections cropped from the original texture images. Similarly, the low-resolution training data is generated by cropping 100×100 sections from the texture images and artificially downsampling it by a predefined forward operator f . The forward operator f is a convolution with a 16×16 Gaussian blur kernel with standard deviation 2, stride 4 and $\xi \sim \mathcal{N}(0, 0.01^2)$ is some noise. Note that the stride determines the subsampling factor in each direction. To keep the dimensions consistent, we use zero-padding. As weighting parameter in the WPP-loss (8) we used $\lambda = 12.5$.⁵

The resulting quality measures are given in Table 1 and the reconstructions are shown in Figure 1 and 2, respectively. We observe that the WPPNet and WPP result into significantly sharper and visually better results than the other methods. However, the WPP requires the minimization of the functional (5) for each reconstruction, which is computationally costly. Also DIP+TV requires for any reconstruction the training of a NN and for PnP-DRUNet, we have to compute the iteration (3) several times. Thus, the reconstruction time for WPP, DIP+TV and PnP-DRUNet is significantly larger than for WPPNet and CNNNet.

Further, we observe that PnP-DRUNet and DIP+TV have a better PSNR value than the WPPNet for the texture "Floor". However, it is well-known that the PSNR as quality measure prefers smooth images. In terms of the blur effect, LPIPS and the visual impression, the WPPNet and WPP are clearly better than the other methods.

5.2 Synchrotron Computed Tomography Data

Next we consider material data which was also used in [24, 26]. A series of multi-scale 3D images has been acquired by synchrotron micro-computed tomography at the SLS beamline TOMCAT. Samples of two materials were selected to provide 3D images having different levels of complexity, namely

- "SiC Diamonds" obtained by microwave sintering of silicon and diamonds, see [56].

³We use the implementation <https://github.com/richzhang/PerceptualSimilarity>, version 0.1.

⁴available at <https://kylberg.org/kylberg-texture-dataset-v-1-0>

⁵The implementation of this example is available online at <https://github.com/FabianAltekrueger/WPPNets>.

		bicubic	PnP-DRUNet	DIP+TV	CNNNat	WPP	WPPNet
Grass	PSNR	22.68	24.71	24.97	25.06	24.61	24.79
	Blur Effect	0.5980	0.4649	0.4410	0.4307	0.4153	0.4219
	LPIPS	0.4891	0.4074	0.2287	0.2403	0.1777	0.2353
Floor	PSNR	29.03	32.96	32.90	30.35	30.39	30.99
	Blur Effect	0.7469	0.6803	0.6690	0.5977	0.5218	0.5407
	LPIPS	0.2568	0.2584	0.2462	0.2795	0.1647	0.1705

Table 1: Comparison of superresolution results for the textures "Grass" and "Floor" (stride 4). The best two values are marked in bolt.

		bicubic	PnP-DRUNet	DIP+TV	CNNNat	WPP	WPPNet
SiC	PSNR	25.34	27.43	27.81	27.66	27.57	27.83
	Blur Effect	0.5794	0.4405	0.3829	0.4046	0.3743	0.3810
	LPIPS	0.4216	0.3133	0.2076	0.2441	0.1627	0.1819
FS	PSNR	29.19	31.05	31.35	31.68	31.07	30.85
	Blur Effect	0.4856	0.4936	0.3724	0.4276	0.3225	0.3299
	LPIPS	0.3524	0.3565	0.2162	0.2441	0.1630	0.1771

Table 2: Comparison of superresolution results for material images with stride 4. The best two values are marked in bolt.

- "FS" (Fontainebleau sandstone), a rather homogeneous natural rock that is commonly used in the oil industry for flow experiments.

In our experiments we consider a voxel spacing of 1.625 μm . From this 3D image we extract 2D slices of size 600×600 and use them as ground truth and reference images for our experiments. Some examples are given in Figure 3. Since we require that the forward operator f is known (same f as in Section 5.1), we generate the low resolution images artificially by extracting 2D slices from our 3D image and downsample it using the known predefined forward operator f . In this way, we generate a set of 1000 low-resolution images of size 25×25 for training the WPPNet.

The resulting quality measures are given in Table 2 and the reconstructions are shown in Figure 4 and 5. Similar as in Subsection 5.1, we observe that the reconstructions with WPPNet and WPP are significantly sharper and visually better than the other methods. Again, the PSNR prefers in some cases the much smoother reconstructions of DIP+TV and CNNNat. However, the results of WPPNet and WPP look visually much better which is also quantified by smaller values for LPIPS and blur effect.

We apply all methods onto a larger test set in Appendix D.

Higher Magnification Factor Additionally to the previous examples, we apply WPP-Nets for superresolution with a magnification factor of 6 onto the SiC Diamonds image. Here, the forward operator f is given by a convolution with a 16×16 Gaussian blur kernel with standard deviation 3, stride 6 and zero-padding. As before, we set the noise to $\xi \sim \mathcal{N}(0, 0.01^2)$. We use the same ground truth and reference image as before, illustrated

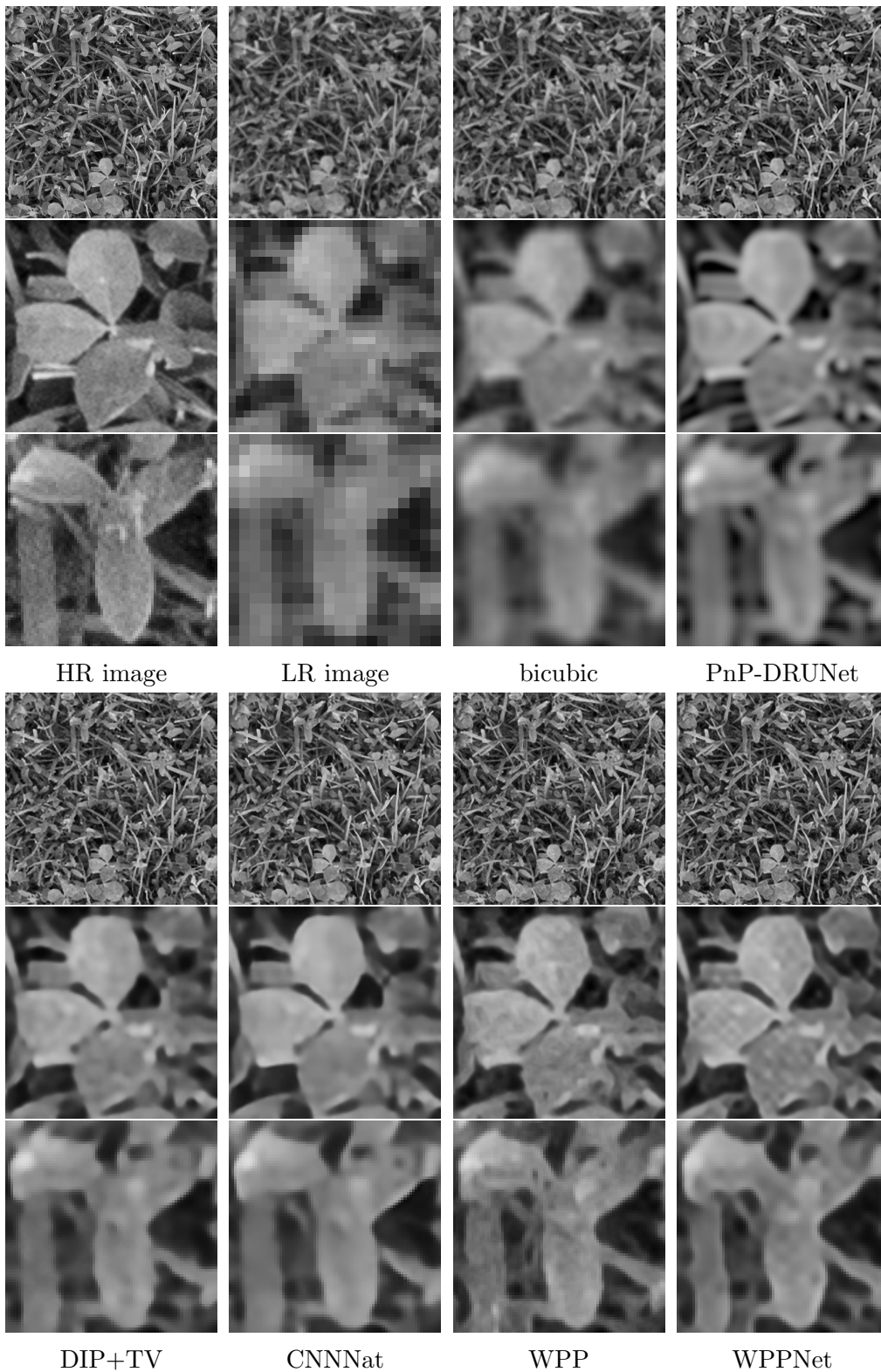


Figure 1: Comparison of superresolution for the texture "Grass" with stride 4.

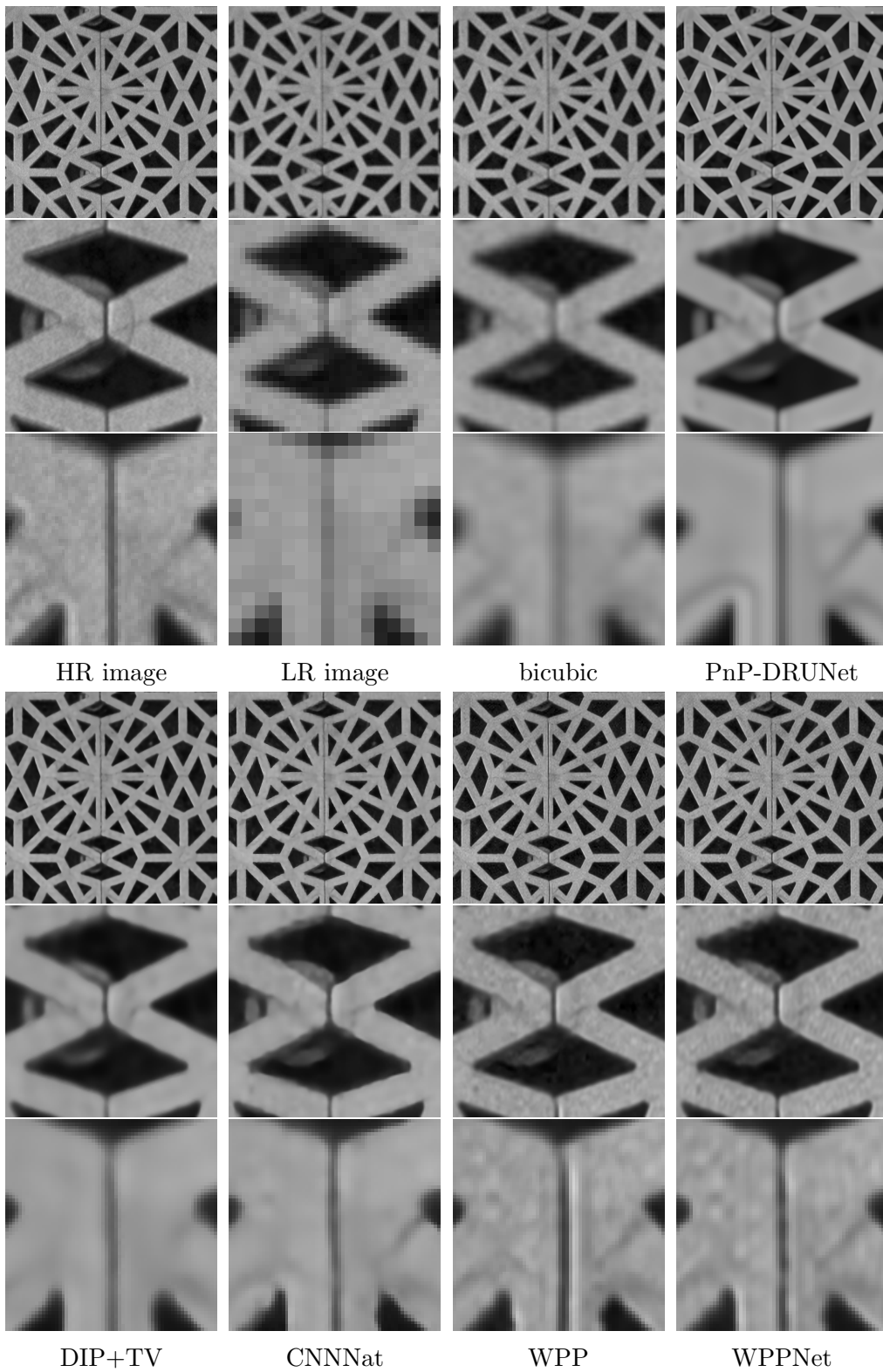


Figure 2: Comparison of superresolution for the texture "Floor" with stride 4.

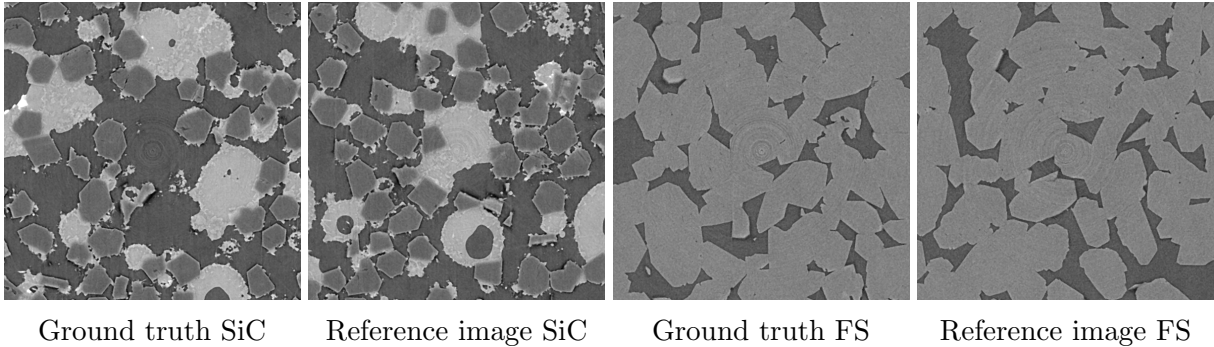


Figure 3: Ground truth and reference image used for the numerical examples.

in Figure 3. The resulting quality measures are given in Table 3 and the reconstructions are shown in Figure 6.

5.3 Stability under Inaccurate Operators

In this subsection, we demonstrate the robustness of WPPNets against inaccurate knowledge of the forward operator f . Our data is given by the SiC Diamonds image.

5.3.1 Inaccurate Forward Operator

In this example, we generate the low-resolution observations using the forward operator f_{true} given by a strided convolution with a 16×16 Gaussian blur kernel with standard deviation 2, stride 4 and zero padding as in the previous subsection. On the other hand, we train the WPPNet and CNNNat with an inaccurate forward operator f_{inacc} , which we also use for the reconstruction with DIP+TV, PnP-DRUNet and WPP. The operator f_{inacc} is given in the same way as f_{true} with the only difference that we use a standard deviation of 2.5.

The resulting quality measures are given in Table 4 and the reconstructions in Figure 7. We observe that WPPNet and WPP are much more robust against the inaccurate operator than all of the comparison methods. While the inaccurate operator leads in CNNNat to unnatural artifacts, it effects a significant blur within the PnP-DRUNet reconstructions. Similarly, in the reconstruction of DIP+TV the edges are blurred. On the other hand, the reconstruction using WPPNet or WPP is still close to the results using the accurate operator from the previous section. Note that CNNNat and DIP+TV have a very small

		bicubic	PnP-DRUNet	DIP+TV	CNNNat	WPP	WPPNet
SiC	PSNR	22.98	24.36	24.82	24.20	24.51	24.44
	Blur Effect	0.6875	0.6139	0.5036	0.4476	0.4081	0.4151
	LIPS	0.5988	0.4987	0.3602	0.3306	0.2497	0.2626

Table 3: Comparison of superresolution results for the material "SiC" with stride 6. The best two values are marked in bolt.

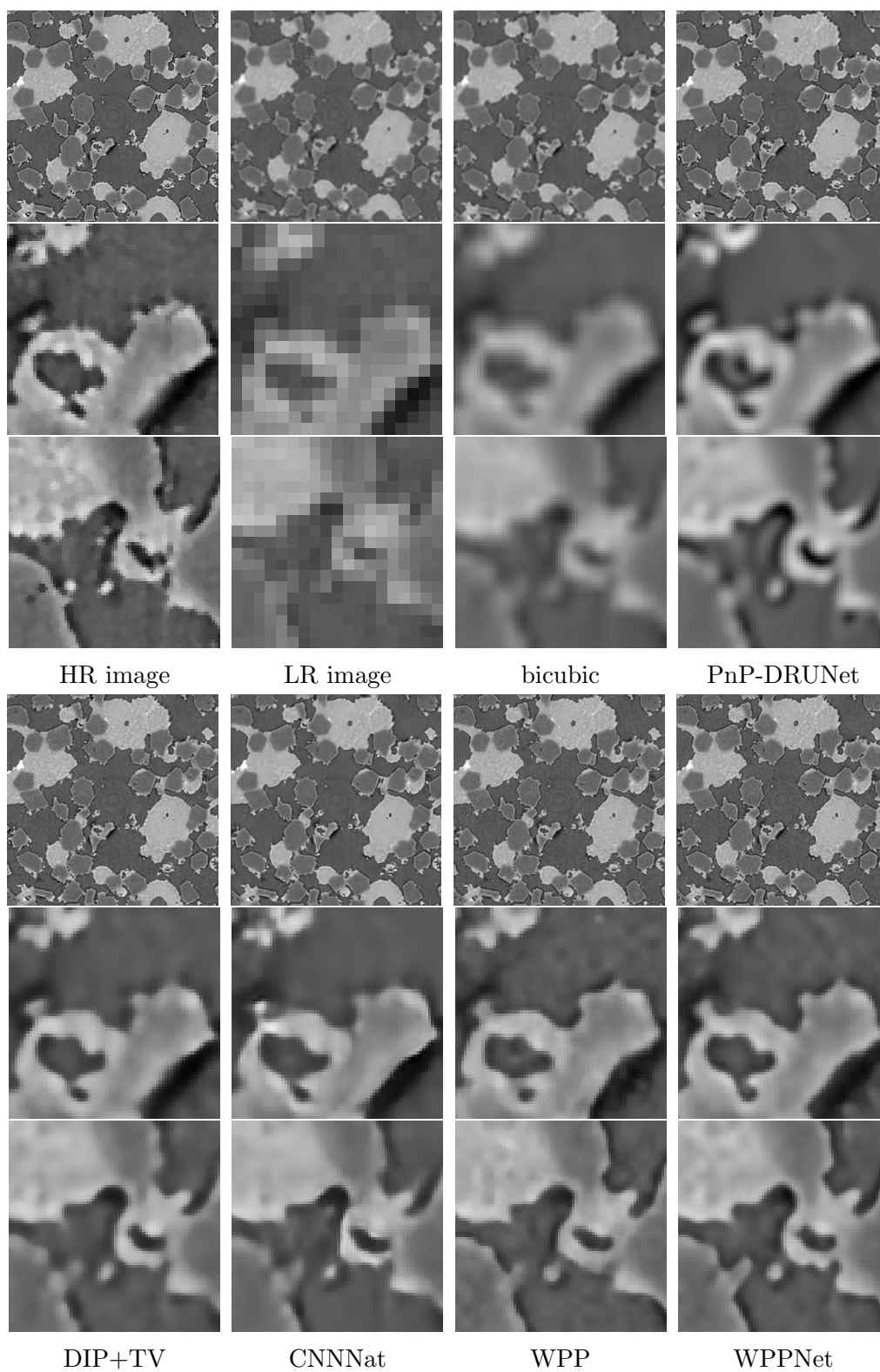


Figure 4: Comparison of superresolution for the material "SiC Diamonds" with stride 4.

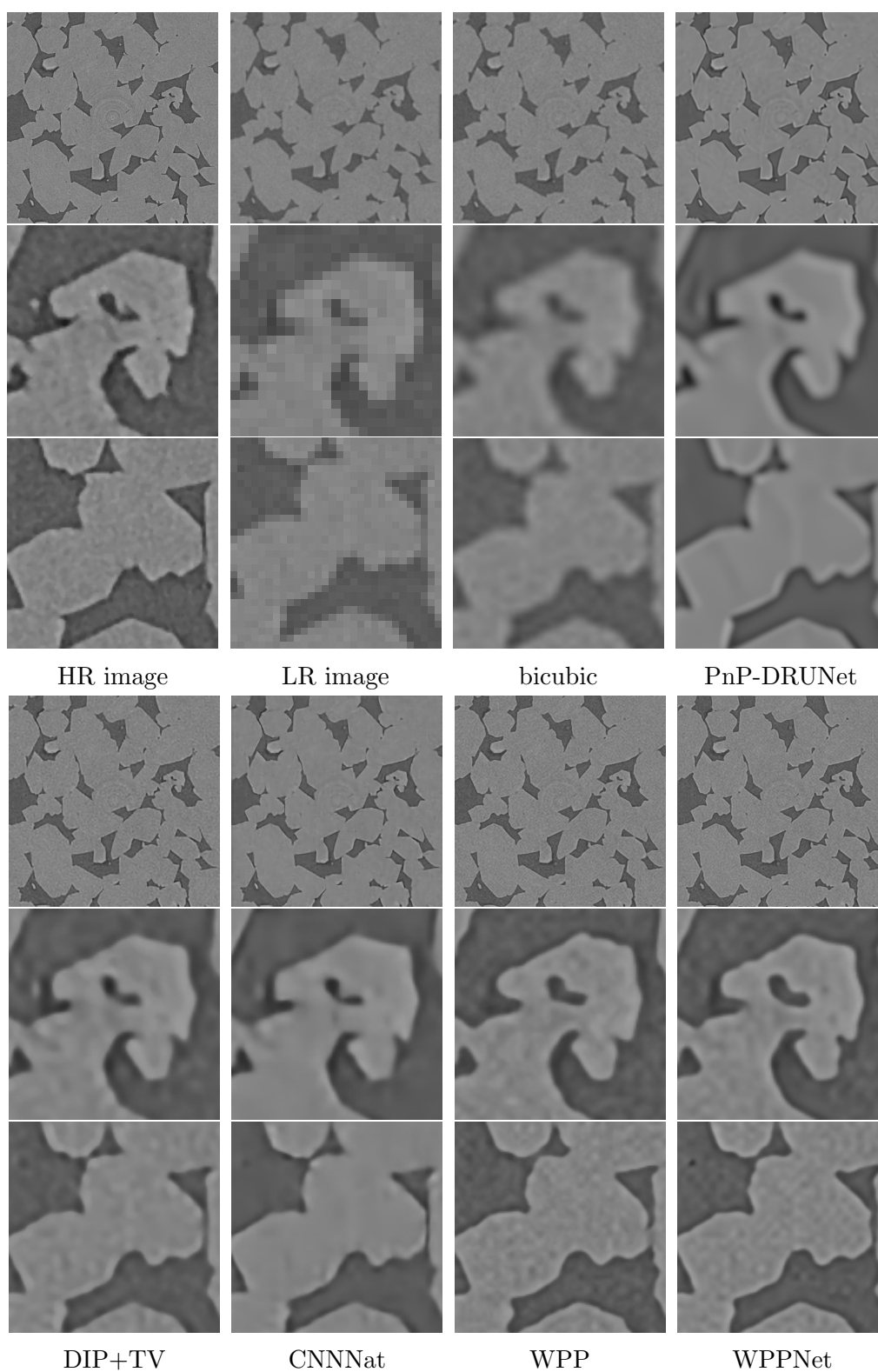


Figure 5: Comparison of superresolution for the material "FS" with stride 4.

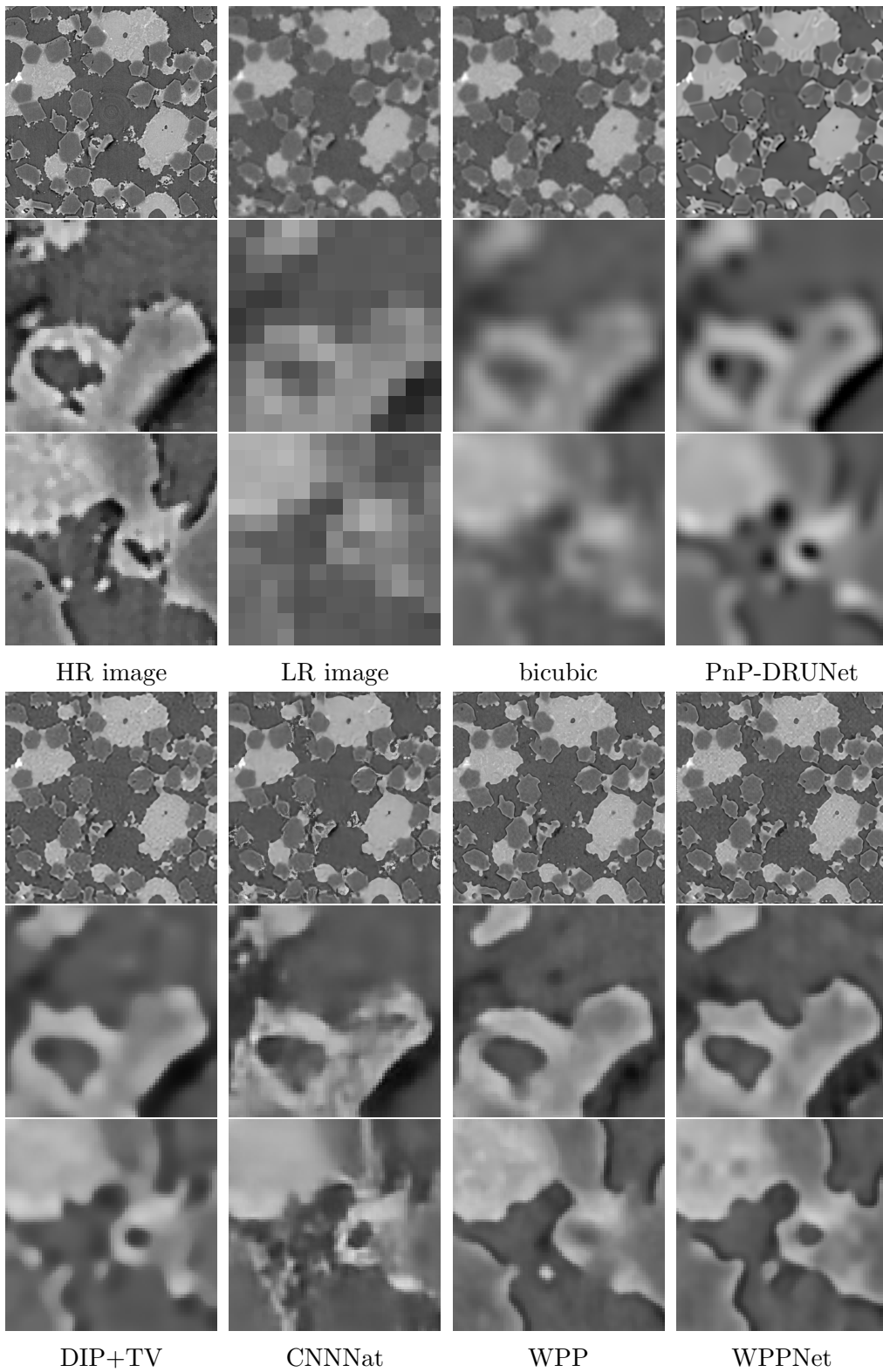


Figure 6: Comparison of superresolution for the material "SiC" with stride 6.

		PnP-DRUNet	DIP+TV	CNNNat	WPP	WPPNet
SiC	PSNR	26.58	26.69	23.29	27.45	27.68
	Blur Effect	0.4367	0.3766	0.3054	0.3876	0.3964
	LPIPS	0.3563	0.2266	0.2495	0.1725	0.2055

Table 4: Comparison of superresolution results for "SiC" with an inaccurate forward blurr operator and stride 4. The best two values are marked in bolt.

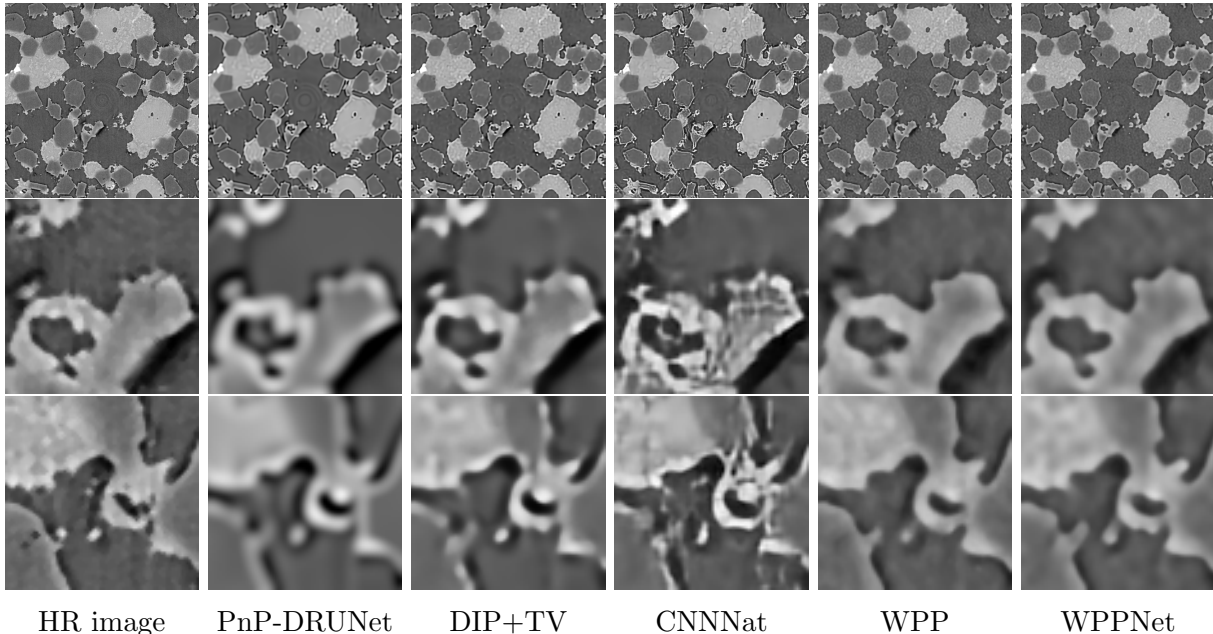


Figure 7: Comparison of superresolution for the material "SiC" with an inaccurate forward blur operator and stride 4.

blur effect. However, this is due to the fact that the reconstruction with CNNNat and DIP+TV contains a large number of high-frequency artifacts.

5.3.2 Estimated Forward Operator

Finally, we aim to evaluate the performance of WPPNets in a real-world setting motivated by the imaging of materials microstructures. We assume that we have scanned a large area from a materials microstructure using a low resolution. Due to the limited amount of time and resources it is not possible to scan the same area with a higher resolution. On the other hand, we assume that we are given a high-resolution image of some small part of this area.

In this setting, we aim to generate a high-resolution correspondence for the whole low-resolution image. We proceed in two steps. First, we estimate the forward operator of the superresolution problem using the small high-resolution part. Second, we reconstruct the high-resolution image using the estimated forward operator.

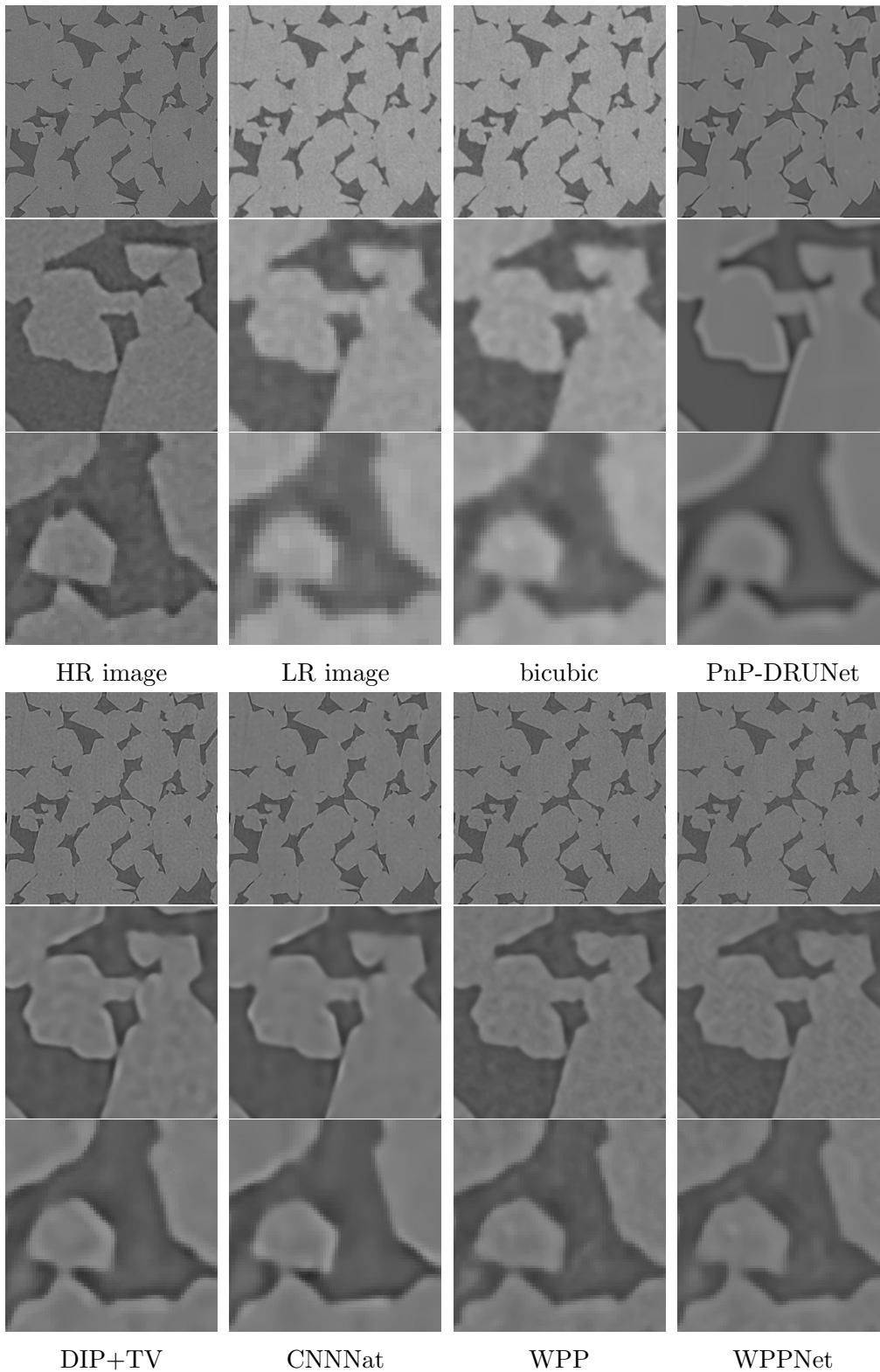


Figure 8: Reconstruction of the high resolution image "Fontainebleau sandstone" assuming the estimated forward operator.

		bicubic	PnP-DRUNet	DIP +TV	CNNNat	WPP	WPPNet
	PSNR	17.67	32.91	32.25	32.97	32.68	32.80
FS	Blur Effect	0.4817	0.4964	0.3900	0.4248	0.3330	0.3197
	LPIPS	0.2805	0.3459	0.2389	0.2882	0.1362	0.1411

Table 5: Comparison of superresolution results using the estimated forward operator. The best two values are marked in bolt.

Data generation and estimation of the Forward Operator Now, we consider the synchrotron-computed tomography data from Section 5.2 and consider the images with voxel spacings $1.625 \mu\text{m}$ and $3.25 \mu\text{m}$.

Here, we extract a large database of low-resolution images (2D slices of the image with voxel spacing $3.25 \mu\text{m}$). Further, we extract two pairs $(\tilde{x}_1, \tilde{y}_1)$ and $(\tilde{x}_2, \tilde{y}_2)$ of 2D-slices from the images with voxel spacings $1.625 \mu\text{m}$ and $3.25 \mu\text{m}$ showing the same area of the material. Here, the \tilde{x}_i are extracted from the image with voxel spacing $1.625 \mu\text{m}$ and the \tilde{y}_i come from the image with voxel spacing $3.25 \mu\text{m}$. The pair $(\tilde{x}_1, \tilde{y}_1)$ will be used for estimating the operator and the image \tilde{x}_1 will serve as a reference image for WPPNet and WPP. Further, we use the pair $(\tilde{x}_2, \tilde{y}_2)$ for evaluating our results, where \tilde{y}_2 is the low-resolution observation, while \tilde{x}_2 is the high-resolution ground truth.

Note that $(\tilde{x}_i, \tilde{y}_i)$ are real-world data. Thus, we register the images $(\tilde{x}_i, \tilde{y}_i)$ in a pre-processing step using the scale-invariant feature transform (SIFT) [39].

In practice, the forward operator could also be estimated from synthetic data (see e.g., [24]), which circumvents the need of the given registered pairs $(\tilde{x}_i, \tilde{y}_i)$. However, generating synthetic data for the synchrotron-computed tomography data is out of scope of our paper.

We estimate the forward operator from the registered pair $(\tilde{x}_1, \tilde{y}_1)$ in the same way as proposed in [24]. For completeness, we describe this procedure in Appendix E.

Results The resulting quality measures are given in Table 5 and the reconstructions are shown in Figure 8. We observe that WPPNet and WPP produce significantly sharper and visually better results than the comparisons. This is also captured by the quality measures. Note that there is a change of contrast and brightness between the high-resolution and the low-resolution image. As the bicubic interpolation does not consider the operator, this results in a brightness difference of the bicubic interpolation to the ground truth.

5.4 Uncertainty Quantification

Finally, we aim to detect the uncertainties within the reconstructions with the WPP. To this end, we consider again the SiC Diamonds images.

Magnification Factor 4 Here we use the same forward operator f as in Section 5.2, thus the same 1000 low-resolution images of size 25×25 are used for training the WPPFlow.

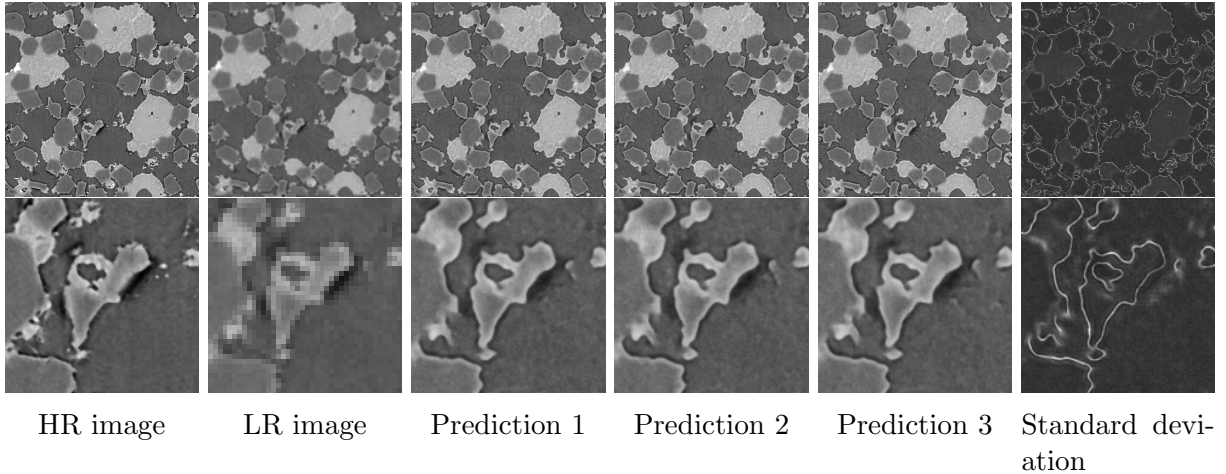


Figure 9: Different reconstructions of the ground truth image with stride 4. *Right*: The normalized standard deviation.

In Figure 9 we show three different high-resolution predictions with a magnification factor 4 given the same low-resolution image. Note that here we considered the same reference image \tilde{x} as in Figure 4. We computed 100 high-resolution predictions and the resulting standard deviation is given in the right part. Here the brighter a pixel is, the less secure is the WPPFlow in its prediction; the maximal pixel-wise standard deviation is 0.08. Obviously, we have a high uncertainty on the edges, while there is nearly no uncertainty in the other regions.

Magnification Factor 8 Additionally, we consider the superresolution task with a magnification factor 8. Here, the forward operator f is given by a convolution with a 16×16 Gaussian blur kernel with standard deviation 4, stride 8 and zero-padding to keep the dimensions consistent. Again, we set the noise to $\xi \sim \mathcal{N}(0, 0.01^2)$. For training we use a generated set consisting of 270 low-resolution images of size 20×20 .

In Figure 10 we show different reconstructions with a magnification factor 8 of a given low-resolution image. Of course, here the differences between the predictions are much larger and we have a higher standard deviation; the maximal pixel-wise standard deviation is 0.167. In contrast to magnification factor 4, where the uncertainties are mainly visible on the edges, in the case of magnification factor 8 the uncertainties are visible on a much larger area. In particular, we observe that WPPFlows are able to detect uncertainties in the topological structure of the data, e.g., if two certain structures are connected or not.

6 Conclusion

We introduced WPPNets, which are CNNs trained with a new loss function based on comparisons of empirical patch distributions via the quadratic Wasserstein distance and demonstrated its power by several numerical examples. In particular, we observed that WPPNets are very stable under inaccurate operators appearing in real-world applications.

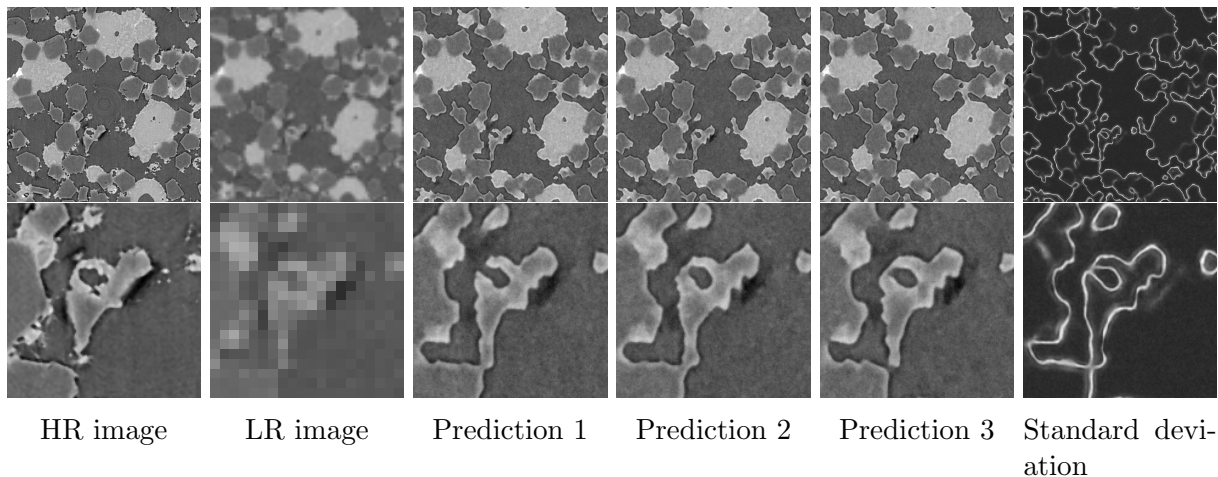


Figure 10: Different reconstructions of the ground truth image with stride 8. *Right*: The normalized standard deviation.

Due to the fact that WPPs require the knowledge of one high-resolution reference image, WPPs could also be interpreted as a method for one-shot learning, see [8, 60] and references therein. However, as no low-resolution correspondence to the reference image is given, we would call our WPP based methods an unsupervised learning method. We measured the uncertainty within the reconstructions by combining WPPs with conditional normalizing flows.

Our considerations could be extended in several directions:

- So far, we focused on image superresolution. However, the same methods can be applied for any inverse problem.
- Other noise models than the Gaussian one can be easily incorporated.
- Images of materials microstructures are often three-dimensional. Thus, in the future, we would extend the architecture of the WPPNets for three-dimensional images.
- Quantitative, mathematical estimates how inaccurate operators influence the results are desirable.

Acknowledgements

Funding by German Research Foundation (DFG) within the project STE 571/16-1 and by the DFG under Germany’s Excellence Strategy – The Berlin Mathematics Research Center MATH+ within the project TP: EF3-7 are gratefully acknowledged. The data from Section 5.2 and the second example in Section 5.3 has been acquired in the frame of the EU Horizon 2020 Marie Skłodowska-Curie Actions Innovative Training Network MUMMERING (MULTiscale, Multimodal and Multidimensional imaging for Engineer-ING, Grant Number 765604) at the beamline TOMCAT of the SLS by A. Saadaldin, D. Bernard, and F. Marone Welford. We acknowledge the Paul Scherrer Institut, Villigen,

Switzerland for provision of synchrotron radiation beamtime at the TOMCAT beamline X02DA of the SLS. Many thanks to Dang Phoung Lan Nguyen for registering the images from the second example in Section 5.3. We would like to thank Gabriele Steidl and Paul Hagemann for fruitful discussions.

A Proof of Proposition 2

By (4), for each $x \in \mathbb{R}^d$ it holds that

$$\begin{aligned} W_2^2(\mu_x, \mu_{\tilde{x}}) &= \max_{\psi \in \mathbb{R}^{\tilde{N}}} \left(\frac{1}{N} \sum_{j=1}^N \psi^c(P_j(x)) + \frac{1}{\tilde{N}} \sum_{k=1}^{\tilde{N}} \psi_k \right) \\ &\geq \frac{1}{N} \sum_{j=1}^N \min_{k \in \{1, \dots, \tilde{N}\}} \|P_j(x) - P_k(\tilde{x})\|_2^2, \end{aligned}$$

using $\psi = 0$. Now, for $x \in \mathbb{R}^d$ and $j \in \{1, \dots, N\}$, let $\kappa(j, x) \in \{1, \dots, \tilde{N}\}$ be one element of $\arg \min_{k \in \{1, \dots, \tilde{N}\}} (\|P_j(x) - P_k(\tilde{x})\|_2^2)$. Moreover, let $j^*(x) \in \arg \max_{j \in \{1, \dots, N\}} \|P_j(x)\|_\infty$ be a patch which contains the entry of x with the largest absolute value. Then we have

$$\begin{aligned} W_2^2(\mu_x, \mu_{\tilde{x}}) &\geq \frac{1}{N} \sum_{j=1}^N \|P_j(x) - P_{\kappa(j,x)}(\tilde{x})\|_2^2 \\ &\geq \frac{1}{N} \|P_{j^*(x)}(x) - P_{\kappa(j^*(x),x)}(\tilde{x})\|_2^2 \\ &= \frac{1}{N} \sum_{l=1}^{p^2} ((P_{j^*(x)}(x))_l - (P_{\kappa(j^*(x),x)}(\tilde{x}))_l)^2, \end{aligned}$$

where p is the patch size. By considering just the summand l with $(P_{j^*(x)}(x))_l = \|x\|_\infty$ and using that $(P_{\kappa(j^*(x),x)}(\tilde{x}))_l \leq \|\tilde{x}\|_\infty$, we obtain

$$W_2^2(\mu_x, \mu_{\tilde{x}}) \geq \frac{1}{N} (\max(\|x\|_\infty - \|\tilde{x}\|_\infty, 0))^2 \geq \frac{1}{N} (\max(c\|x\|_2 - \|\tilde{x}\|_\infty, 0))^2,$$

for some $c > 0$. Now define the compact set $K = \{x \in \mathbb{R}^d : \|x\|_2 \leq \frac{4}{c} \|\tilde{x}\|_\infty\}$. Then, it holds for all $x \in \mathbb{R}^d \setminus K$ that

$$(\max(c\|x\|_2 - \|\tilde{x}\|_\infty, 0))^2 = (c\|x\|_2 - \|\tilde{x}\|_\infty)^2 \quad \text{and} \quad \frac{c^2}{2} \|x\|_2^2 - 2c\|x\|_2 \|\tilde{x}\|_\infty \geq 0. \quad (11)$$

We can split the integral over φ as

$$\int_{\mathbb{R}^d} |\varphi(x)| dx = \int_K |\varphi(x)| dx + \int_{\mathbb{R}^d \setminus K} |\varphi(x)| dx.$$

Since the Wasserstein distance is non-negative, we have that $|\varphi(x)| \leq 1$. As K is compact, we obtain that the first summand in the above formula is finite. It remains to show that also the second summand is finite. Indeed, it holds

$$\begin{aligned} \int_{\mathbb{R}^d \setminus K} |\varphi(x)| dx &= \int_{\mathbb{R}^d \setminus K} \exp(-\rho W_2^2(\mu_x, \mu_{\tilde{x}})) dx \\ &\leq \int_{\mathbb{R}^d \setminus K} \exp\left(-\frac{\rho}{N} (\max(c\|x\|_2 - \|\tilde{x}\|_\infty, 0))^2\right) dx. \end{aligned}$$

Since we are integrating over all x outside from K , we obtain by (11) that

$$\begin{aligned} \int_{\mathbb{R}^d \setminus K} |\varphi(x)| dx &\leq \int_{\mathbb{R}^d \setminus K} \exp\left(-\frac{\rho}{N} (c^2\|x\|_2^2 - 2c\|x\|_2\|\tilde{x}\|_\infty + \|\tilde{x}\|_\infty^2)\right) dx \\ &\leq \int_{\mathbb{R}^d \setminus K} \exp\left(-\frac{\rho}{2N} c^2\|x\|_2^2\right) \exp\left(-\frac{\rho}{N} \underbrace{(c^2\|x\|_2^2 - 2c\|x\|_2\|\tilde{x}\|_\infty)}_{\geq 0 \text{ by (11)}}\right) dx \\ &\leq \int_{\mathbb{R}^d \setminus K} \exp\left(-\frac{\rho}{2N} c^2\|x\|_2^2\right) dx < \infty. \end{aligned}$$

This finishes the proof. \square

B Implementation details of WPPNets

All experiments are implemented in PyTorch. We run them on a single NVIDIA GeForce RTX 2060 GPU with 6 GB GPU memory.

Network Architecture We use a 16-layer CNN G_θ which is adapted from [54]. In [54] the authors propose a so-called asymmetric CNN (ACNN) for image super-resolution consisting of 23-layers. More specifically, the ACNN has a 17-layer asymmetric block, a 1-layer memory enhancement block and a 5-layer high-frequency feature enhancement block (for more details about the structure and the tasks of the individual blocks, see [54, Section III]). As stated above, we modified the proposed ACNN and take a 10-layer asymmetric block (instead of 17-layer) in order to reduce the network complexity.

Training Details For the training of the WPPNet we use the Adam optimizer [31] with a learning rate of 0.0001. The training and test data is independently chosen; we used 1000 low-resolution images of size 25×25 for training the network and have two pairs of validation images of size 600×600 and 150×150 for the high- and low-resolution image, respectively. For the training process the batch size is set to 25 and the number of epochs we trained for the reconstruction image is stated in Table 6. We choose the patch size to be $p = 6$, i.e., $P_i(x)$ is a small sub-image of size 6×6 of an image x .

To obtain an approximation of the maximizer ψ^* of F we use 20 iterations (except for Figure 1, there we used 10 iterations) of a stochastic gradient ascent with a learning rate of 1. Moreover, instead of starting with an arbitrary ψ_l^0 or choosing $\psi_l^0 = 0$ for

the optimization in epoch l , we save the approximated maximizer ψ_{l-1}^{20} from the previous epoch $l - 1$ and use it as the starting vector in epoch l , i.e., $\psi_{l-1}^{20} = \psi_l^0$. Herewith we reach a better approximation of the maximizer ψ_l^* in a computationally efficient way.

C Implementation Details for WPPFlows

Network Architecture The conditional normalizing flow is adapted from [40]. Here the authors propose a multiscale normalizing flow with 3 and 4 scales for a magnification factor 4 and 8, respectively, consisting of 16 flow steps, followed by a transition step for learning a better transition between the scales. Moreover, as a conditioning network a standard 23-block RRDB architecture [59] is used to extract features from the given low-resolution image.

We modified the network to reduce the complexity. In particular, we do not use a conditioning network, but we use the low-resolution image itself and their bicubic interpolations for the respective scale. The input from the latent space $z \sim p_z$ is of the same size as the high-resolution reconstruction and then invertible reshaped to the size of the low-resolution. The downsample step is taken from [12], which consists of an invertible reshaping, followed by a GlowCoupling block and an Actnorm layer. Then, as in [40], 16 and 10 flow steps and a transition step follow for magnification factor 4 and 8, respectively. Lastly, a conditional affine transform in the high resolution scale is used. Note that we do not use a splitting of 50 % in the channel dimension and we only use 2 and 3 scales for a magnification factor 4 and 8, respectively.

Training Details Similar to WPPNet, we used the Adam optimizer [31] with a learning rate of 0.0001. While 1000 low-resolution images of size 25×25 are used for training WPPFlow with a magnification factor 4, for the magnification factor 8 we used 270 low-resolution images of size 20×20 . For the training process the batch size is set to 10, the patch size is chosen to be 6 and both networks are trained for 450 epochs. We use the regularization parameter $\lambda = 100$ and the maximizer ψ^* is computed similar to WPPNets.

D Evaluation on a Larger Test Set

In order to make the experiments from Section 5.2 more reliable, we apply the different methods onto a larger test set. Three exemplar images from the test set are given in Figure 11. The average of the errors are given in Table 7. Again, the WPPNet and WPP perform

	Figure 1	Figure 2	Figure 4	Figure 5	Figure 6	Figure 7	Figure 8
epochs	420	270	450	420	570	420	150

Table 6: Number of epochs to obtain the reconstructions visualized in the respective Figure.

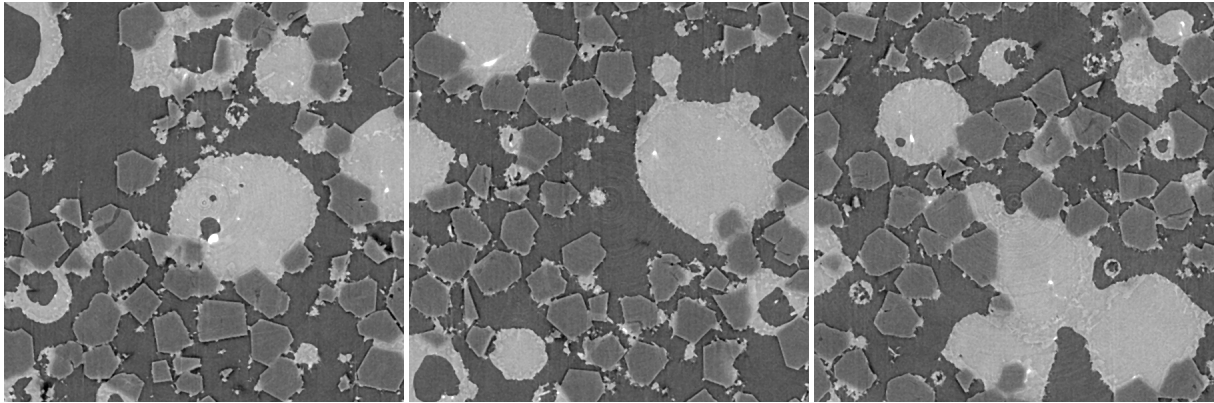


Figure 11: Exemplary ground truth images used for further numerical examples.

		bicubic	PnP-DRUNet	DIP+TV	CNNat	WPP	WPPNet
SiC	PSNR	25.70	27.72	28.04	28.00	27.72	28.00
	Blur Effect	0.5342	0.4455	0.3802	0.3967	0.3596	0.3663
	LPIPS	0.4110	0.3265	0.2141	0.2272	0.1591	0.1830

Table 7: Averaged PSNR, Blur Effect and LPIPS value of the high-resolution reconstructions. The best two values are marked in bolt.

better than the other methods in terms of the considered quality measures. Overall, the results are comparable with the results from Section 5.2.

E Estimation of the Forward Operator

In the following, we describe the estimation process of the forward operator f for super-resolution, which is used in the second example of Section 5.3. For the estimation, we assume that we have given a registered pair (\tilde{x}, \tilde{y}) of a high-resolution and a low-resolution image and follow the lines of [24].

We assume that our forward operator is given by $f(x) = S(k * x + b)$ for a 15×15 blur kernel k , a bias $b \in \mathbb{R}$ and a downsampling operator S .

Definition of the downsampling operator Further, for the downsampling operator S , we make use of Fourier transforms. Given an image $x \in \mathbb{R}^{n_x, n_y}$ the two-dimensional discrete Fourier transform (DFT) is defined by $\mathcal{F}_{n_x, n_y} := \mathcal{F}_{n_x} \otimes \mathcal{F}_{n_y}$, where we have $\mathcal{F}_n = (\exp(-2\pi ikl/n))_{k,l=0}^{n-1}$. Now, the downsampling operator $S: \mathbb{R}^{m_x, m_y} \rightarrow \mathbb{R}^{n_x, n_y}$ is given by

$$S = \frac{n_x n_y}{m_x m_y} \mathcal{F}_{n_x, n_y}^{-1} D \mathcal{F}_{m_x, m_y},$$

where for $x \in \mathbb{C}^{m_x, m_y}$ the (i, j) -th entry of $D(x)$ is given by $x_{i', j'}$, where

$$i' = \begin{cases} i, & \text{if } i \leq \frac{n_x}{2}, \\ i + m_x - n_x, & \text{otherwise.} \end{cases}$$

and j' is defined analogously. Thus, the operator S generates a downsampled version $S(x)$ of an image x by removing the high-frequency part from x . Note that even if the Fourier matrix \mathcal{F}_{n_x, n_y} is complex valued, the range of S is real-valued, as D preserves Hermitian-symmetric spectra.

Estimation of Blur Kernel and Bias We assume that we have given images $\tilde{x} \in \mathbb{R}^{m_x, m_y}$ and $\tilde{y} \in \mathbb{R}^{n_x, n_y}$ related by $\tilde{y} \approx S(k * \tilde{x} + b)$, where the blur kernel $k \in \mathbb{R}^{15 \times 15}$ and the bias $b \in \mathbb{R}$ are unknown. In the following, we aim to reconstruct k and b from \tilde{x} and \tilde{y} . Here, we use the notations $N = n_x n_y$ and $M = m_x m_y$. Further let $\tilde{k} \in \mathbb{R}^{m_x, m_y}$ be the kernel k padded with zeros such that it still corresponds to the same convolution as k , but has size $m_x \times m_y$.

Applying the DFT on both sides of $y = S(k * \tilde{x} + b) = S(\tilde{k} * \tilde{x} + b)$ and using the definition of S , we obtain that

$$\hat{y} = \frac{N}{M} D(\hat{k} \odot \hat{x} + Mbe) = \frac{N}{M} D(\hat{k}) \odot D(\hat{x}) + Nbe,$$

where $\hat{y} = \mathcal{F}_{n_x, n_y} \tilde{y}$, $\hat{x} = \mathcal{F}_{m_x, m_y} \tilde{x}$, $\hat{k} = \mathcal{F}_{m_x, m_y} \tilde{k}$, \odot is the elementwise product and e denotes the first unit vector (i.e., $e_{0,0} = 1$ and all other entries are zero). Now, we can conclude that

$$D(\hat{k}) = \frac{M}{N} \hat{y} \oslash D(\hat{x}) - \frac{Mb}{\hat{x}_{0,0}} e,$$

where \oslash is the elementwise quotient. In practice, we stabilize this quotient by increasing the absolute value of $D(\hat{x})$ by 10^{-5} while retaining the phase. Thus, assuming that the high-frequency part of k is negligible (i.e., that $D^T D k = k$), we can approximate \hat{k} by

$$\hat{k} \approx \frac{M}{N} D^T \hat{y} \oslash D(\hat{x}) - \frac{Mb}{\hat{x}_{0,0}} e.$$

Applying the inverse DFT this becomes

$$\tilde{k} \approx \mathcal{F}_{m_x, m_y}^{-1} \left(\frac{M}{N} D^T (\hat{y} \oslash D(\hat{x})) \right) - \frac{b}{\hat{x}_{0,0}}.$$

Using the assumption that \tilde{k} is zero outside of the 15×15 patch, where k is located, we can estimate b by taking the mean over all pixels of $\mathcal{F}_{m_x, m_y}^{-1} \left(\frac{M}{N} D^T (\hat{y} \oslash D(\hat{x})) \right)$ outside of this 15×15 patch. Afterwards, we estimate k by reprojecting

$$\mathcal{F}_{m_x, m_y}^{-1} \left(\frac{M}{N} D^T (\hat{y} \oslash D(\hat{x})) \right) - \frac{b}{\hat{x}_{0,0}}$$

to the set of all real 15×15 kernels.

References

- [1] A. Andriele, N. Farchmin, P. Hagemann, S. Heidenreich, V. Soltwisch, and G. Steidl. Invertible neural networks versus MCMC for posterior reconstruction in grazing incidence X-ray fluorescence. In *International Conference on Scale Space and Variational Methods in Computer Vision*, pages 528–539. Springer, 2021.
- [2] L. Ardizzone, J. Kruse, C. Lüth, N. Bracher, C. Rother, and U. Köthe. Conditional invertible neural networks for diverse image-to-image translation. In *Pattern Recognition: 42nd DAGM German Conference, DAGM GCP 2020, Tübingen, Germany, September 28 – October 1, 2020, Proceedings*, page 373–387, Berlin, Heidelberg, 2020. Springer-Verlag.
- [3] L. Ardizzone, J. Kruse, C. Rother, and U. Köthe. Analyzing inverse problems with invertible neural networks. In *7th International Conference on Learning Representations, ICLR 2019, New Orleans, LA, USA, May 6-9, 2019*, 2019.
- [4] D. O. Bagueer, J. Leuschner, and M. Schmidt. Computed tomography reconstruction using deep image prior and learned reconstruction methods. *Inverse Problems*, 36, 2020.
- [5] A. Buades, B. Coll, and J.-M. Morel. A non-local algorithm for image denoising. In *2005 IEEE Computer Society Conference on Computer Vision and Pattern Recognition*, volume 2, pages 60–65. IEEE, 2005.
- [6] S. H. Chan, X. Wang, and O. A. Elgandy. Plug-and-play ADMM for image restoration: Fixed-point convergence and applications. *IEEE Transactions on Computational Imaging*, 3(1):84–98, 2016.
- [7] R. Chen, J. Behrmann, D. K. Duvenaud, and J.-H. Jacobsen. Residual flows for invertible generative modeling. In *Advances in Neural Information Processing Systems*, volume 32. Curran Associates, Inc., 2019.
- [8] J. Cheng, Z. Han, Z. Wang, and L. Chen. “One-shot” super-resolution via backward style transfer for fast high-resolution style transfer. *IEEE Signal Processing Letters*, 28:1485–1489, 2021.
- [9] P. L. Combettes and V. R. Wajs. Signal recovery by proximal forward-backward splitting. *Multiscale Modeling & Simulation*, 4(4):1168–1200, 2005.
- [10] L. Condat, D. Kitahara, A. Contreras, and A. Hirabayashi. Proximal splitting algorithms: Relax them all. *arXiv preprint arXiv:1912.00137*, 2019.
- [11] F. Crete, T. Dolmiere, P. Ladret, and M. Nicolas. The blur effect: perception and estimation with a new no-reference perceptual blur metric. In *Human vision and electronic imaging XII*, volume 6492, page 64920I. International Society for Optics and Photonics, 2007.

- [12] A. Denker, M. Schmidt, J. Leuschner, and P. Maass. Conditional invertible neural networks for medical imaging. *Journal of Imaging*, 7(11), 2021.
- [13] L. Dinh, J. Sohl-Dickstein, and S. Bengio. Density estimation using real NVP. In *5th International Conference on Learning Representations, ICLR 2017, Toulon, France, April 24-26, 2017, Conference Track Proceedings*, 2017.
- [14] C. Dong, C. C. Loy, K. He, and X. Tang. Image super-resolution using deep convolutional networks. *IEEE Transactions on Pattern Analysis and Machine Intelligence*, 38(2):295–307, 2015.
- [15] J. Eckstein and D. P. Bertsekas. On the Douglas—Rachford splitting method and the proximal point algorithm for maximal monotone operators. *Mathematical Programming*, 55(1):293–318, 1992.
- [16] A. Effland, E. Kobler, K. Kunisch, and T. Pock. Variational networks: An optimal control approach to early stopping variational methods for image restoration. *Journal of Mathematical Imaging and Vision*, 62(3):396, 2020.
- [17] A. A. Efros and T. K. Leung. Texture synthesis by non-parametric sampling. In *Proceedings of the seventh IEEE International Conference on Computer Vision*, volume 2, pages 1033–1038. IEEE, 1999.
- [18] C. Etmann, R. Ke, and C.-B. Schönlieb. iunets: learnable invertible up-and down-sampling for large-scale inverse problems. In *2020 IEEE 30th International Workshop on Machine Learning for Signal Processing (MLSP)*, pages 1–6. IEEE, 2020.
- [19] R. Friedman and Y. Weiss. Posterior sampling for image restoration using explicit patch priors. *arXiv preprint arXiv:2104.09895*, 2021.
- [20] H. Gupta, K. H. Jin, H. Q. Nguyen, M. T. McCann, and M. Unser. CNN-based projected gradient descent for consistent CT image reconstruction. *IEEE Transactions on Medical Imaging*, 37(6):1440–1453, 2018.
- [21] J. Gutierrez, J. Rabin, B. Galerne, and T. Hurtut. Optimal patch assignment for statistically constrained texture synthesis. In *International Conference on Scale Space and Variational Methods in Computer Vision*, pages 172–183. Springer, 2017.
- [22] P. Hagemann, J. Hertrich, and G. Steidl. Generalized normalizing flows via Markov chains. *arXiv preprint arXiv:2111.12506*, 2021.
- [23] P. Hagemann, J. Hertrich, and G. Steidl. Stochastic normalizing flows for inverse problems: a Markov Chains viewpoint. *ArXiv 2109.11375*, 2021.
- [24] J. Hertrich, A. Houdard, and C. Redenbach. Wasserstein patch prior for image superresolution. *arXiv preprint arXiv:2109.12880*, 2021.
- [25] J. Hertrich, S. Neumayer, and G. Steidl. Convolutional proximal neural networks and plug-and-play algorithms. *Linear Algebra and its Applications*, 631:203–234, 2021.

- [26] J. Hertrich, D. P. L. Nguyen, J.-F. Aujol, D. Bernard, Y. Berthoumieu, A. Saadaldin, and G. Steidl. PCA reduced Gaussian mixture models with applications in super-resolution. *Inverse Problems & Imaging*, 2021.
- [27] A. Houdard, C. Bouveyron, and J. Delon. High-dimensional mixture models for unsupervised image denoising (HDMI). *SIAM Journal on Imaging Sciences*, 11(4):2815–2846, 2018.
- [28] A. Houdard, A. Leclaire, N. Papadakis, and J. Rabin. A generative model for texture synthesis based on optimal transport between feature distributions. *arXiv preprint arXiv:2007.03408*, 2021.
- [29] A. Houdard, A. Leclaire, N. Papadakis, and J. Rabin. Wasserstein generative models for patch-based texture synthesis. In A. Elmoataz, J. Fadili, Y. Quéau, J. Rabin, and L. Simon, editors, *Scale Space and Variational Methods in Computer Vision*, page 269–280, Cham, 2021. Springer International Publishing.
- [30] R. Keys. Cubic convolution interpolation for digital image processing. *IEEE Transactions on Acoustics, Speech, and Signal Processing*, 29(6):1153–1160, 1981.
- [31] D. P. Kingma and J. Ba. Adam: A method for stochastic optimization. In *International Conference on Learning Representations*, 2015.
- [32] D. P. Kingma and P. Dhariwal. Glow: Generative flow with invertible 1x1 convolutions. *Advances in neural information processing systems*, 31, 2018.
- [33] E. Kobler, A. Effland, K. Kunisch, and T. Pock. Total deep variation for linear inverse problems. In *Proceedings of the IEEE/CVF Conference on Computer Vision and Pattern Recognition*, pages 7549–7558, 2020.
- [34] J. Kruse, G. Detommaso, R. Scheichl, and U. Köthe. Hint: Hierarchical invertible neural transport for density estimation and bayesian inference. *arXiv preprint arXiv:1905.10687v1*, 2019.
- [35] G. Kylberg. *The Kylberg texture dataset v. 1.0*. Centre for Image Analysis, Swedish University of Agricultural Sciences and Uppsala University, 2011.
- [36] M. Lebrun, A. Buades, and J.-M. Morel. A nonlocal Bayesian image denoising algorithm. *SIAM Journal on Imaging Sciences*, 6(3):1665–1688, 2013.
- [37] A. Leclaire and J. Rabin. A fast multi-layer approximation to semi-discrete optimal transport. In *International Conference on Scale Space and Variational Methods in Computer Vision*, pages 341–353. Springer, 2019.
- [38] B. Lim, S. Son, H. Kim, S. Nah, and K. Mu Lee. Enhanced deep residual networks for single image super-resolution. In *Proceedings of the IEEE Conference on Computer Vision and Pattern Recognition workshops*, pages 136–144, 2017.

- [39] D. G. Lowe. Object recognition from local scale-invariant features. In *Proceedings of the seventh IEEE International Conference on Computer Vision*, volume 2, pages 1150–1157. IEEE, 1999.
- [40] A. Lugmayr, M. Danelljan, L. Van Gool, and R. Timofte. SRFlow: Learning the super-resolution space with normalizing flow. In *ECCV*, 2020.
- [41] D. Martin, C. Fowlkes, D. Tal, and J. Malik. A database of human segmented natural images and its application to evaluating segmentation algorithms and measuring ecological statistics. In *Proceedings of the International Conference on Computer Vision*, volume 2, pages 416–423, July 2001.
- [42] T. Meinhardt, M. Moller, C. Hazirbas, and D. Cremers. Learning proximal operators: Using denoising networks for regularizing inverse imaging problems. In *Proceedings of the IEEE International Conference on Computer Vision*, pages 1781–1790, 2017.
- [43] S. Ono. Primal-dual plug-and-play image restoration. *IEEE Signal Processing Letters*, 24(8):1108–1112, 2017.
- [44] S. Parameswaran, C. Deledalle, L. Denis, and T. Q. Nguyen. Accelerating GMM-based patch priors for image restoration: Three ingredients for a 100x speed-up. *IEEE Transactions on Image Processing*, 28(2):687–698, 2019.
- [45] T. Pinetz, E. Kobler, T. Pock, and A. Effland. Shared prior learning of energy-based models for image reconstruction. *SIAM Journal on Imaging Sciences*, 14(4):1706–1748, 2021.
- [46] D. Rezende and S. Mohamed. Variational inference with normalizing flows. In *International conference on machine learning*, pages 1530–1538. PMLR, 2015.
- [47] Y. Romano, M. Elad, and P. Milanfar. The little engine that could: Regularization by denoising (RED). *SIAM Journal on Imaging Sciences*, 10(4):1804–1844, 2017.
- [48] Y. Romano, J. Isidoro, and P. Milanfar. RAISR: Rapid and accurate image super resolution. *IEEE Transactions on Computational Imaging*, 3(1):110–125, 2017.
- [49] C. Saharia, J. Ho, W. Chan, T. Salimans, D. J. Fleet, and M. Norouzi. Image super-resolution via iterative refinement. *arXiv preprint arXiv:2104.07636*, 2021.
- [50] P. Sandeep and T. Jacob. Single image super-resolution using a joint GMM method. *IEEE Transactions on Image Processing*, 25(9):4233–4244, 2016.
- [51] H. Shi, Y. Traonmilin, and J.-F. Aujol. Compressive learning for patch-based image denoising. *HAL preprint hal-03429102*, 2021.
- [52] A. Shocher, N. Cohen, and M. Irani. “Zero-shot” super-resolution using deep internal learning. In *Proceedings of the IEEE Conference on Computer Vision and Pattern Recognition*, pages 3118–3126, 2018.

- [53] H. Sun and K. L. Bouman. Deep probabilistic imaging: Uncertainty quantification and multi-modal solution characterization for computational imaging, 2020.
- [54] C. Tian, Y. Xu, W. Zuo, C.-W. Lin, and D. Zhang. Asymmetric CNN for image superresolution. *IEEE Transactions on Systems, Man, and Cybernetics: Systems*, 2021.
- [55] D. Ulyanov, A. Vedaldi, and V. Lempitsky. Deep image prior. In *Proceedings of the IEEE Conference on Computer Vision and Pattern Recognition*, pages 9446–9454, 2018.
- [56] S. Vaucher, P. Unifantowicz, C. Ricard, L. Dubois, M. Kuball, J.-M. Catala-Civera, D. Bernard, M. Stampanoni, and R. Nicula. On-line tools for microscopic and macroscopic monitoring of microwave processing. *Physica B: Condensed Matter*, 398(2):191–195, 2007.
- [57] S. V. Venkatakrisnan, C. A. Bouman, and B. Wohlberg. Plug-and-play priors for model based reconstruction. In *2013 IEEE Global Conference on Signal and Information Processing*, pages 945–948. IEEE, 2013.
- [58] X. Wang, K. Yu, S. Wu, J. Gu, Y. Liu, C. Dong, Y. Qiao, and C. Change Loy. ESRGAN: Enhanced super-resolution generative adversarial networks. In *Proceedings of the European Conference on Computer Vision (ECCV) workshops*, pages 0–0, 2018.
- [59] X. Wang, K. Yu, S. Wu, J. Gu, Y. Liu, C. Dong, Y. Qiao, and C. C. Loy. Esrgan: Enhanced super-resolution generative adversarial networks. In L. Leal-Taixé and S. Roth, editors, *Computer Vision – ECCV 2018 Workshops*, pages 63–79, Cham, 2019. Springer International Publishing.
- [60] Y. Wang, Q. Yao, J. T. Kwok, and L. M. Ni. Generalizing from a few examples: A survey on few-shot learning. *ACM Computing Surveys*, 53(3), 2020.
- [61] Z. Wang, J. Chen, and S. C. Hoi. Deep learning for image super-resolution: A survey. *IEEE Transactions on Pattern Analysis and Machine Intelligence*, 2020.
- [62] K. Zhang, Y. Li, W. Zuo, L. Zhang, L. Van Gool, and R. Timofte. Plug-and-play image restoration with deep denoiser prior. *IEEE Transactions on Pattern Analysis and Machine Intelligence*, 2021.
- [63] R. Zhang, P. Isola, A. A. Efros, E. Shechtman, and O. Wang. The unreasonable effectiveness of deep features as a perceptual metric. In *Proceedings of the IEEE Conference on Computer Vision and Pattern Recognition*, pages 586–595, 2018.
- [64] Y. Zhang, Y. Tian, Y. Kong, B. Zhong, and Y. Fu. Residual dense network for image super-resolution. In *Proceedings of the IEEE Conference on Computer Vision and Pattern Recognition*, pages 2472–2481, 2018.

- [65] D. Zoran and Y. Weiss. From learning models of natural image patches to whole image restoration. In *IEEE International Conference on Computer Vision*, pages 479–486. IEEE, 2011.